A generalized law for brittle deformation of Westerly granite

David A. Lockner

U.S. Geological Survey, Menlo Park, California

Abstract. A semiempirical constitutive law is presented for the brittle deformation of intact Westerly granite. The law can be extended to larger displacements, dominated by localized deformation, by including a displacement-weakening break-down region terminating in a frictional sliding regime often described by a rate- and state-dependent constitutive law. The intact deformation law, based on an Arrhenius type rate equation, relates inelastic strain rate to confining pressure P_c, differential stress σ_Δ, inelastic strain ε_i and temperature T. The basic form of the law for deformation prior to fault nucleation is $\ln \dot{\varepsilon}_i = c - (E^*/RT) + (\sigma_\Delta/a\sigma_o)\sin^{-\alpha}(\pi\varepsilon_i/2\varepsilon_o)$ where σ_o and ε_o are normalization constants (dependent on confining pressure), a is rate sensitivity of stress, and α is a shape parameter. At room temperature, eight experimentally determined coefficients are needed to fully describe the stress-strain-strain rate response for Westerly granite from initial loading to failure. Temperature dependence requires apparent activation energy ($E^* \sim 90$ kJ/mol) and one additional experimentally determined coefficient. The similarity between the prefailure constitutive law for intact rock and the rate- and state-dependent friction laws for frictional sliding on fracture surfaces suggests a close connection between these brittle phenomena.

1. Introduction

In this paper we present a semiempirical constitutive law for the brittle deformation of Westerly granite. This generalized rheologic model has a remarkably simple form considering that it describes the interdependence of stress, strain, strain rate, temperature and confining pressure for laboratory samples from initial loading to sample failure. We also extend the law to describe localized deformation processes associated with fault formation and frictional sliding. In this way, the full deformation history, from initial elastic loading to frictional sliding, can be described. Westerly granite was used as a "model" rock in this study because it is a fine-grained, uniform, nearly isotropic rock that has an extensive history of laboratory testing and can provide a high level of repeatability under carefully controlled test conditions. In principle, the deformation law can be adapted easily to other rock types.

The Mohr failure envelope (Figure 1) is a common failure criterion used to relate shear and normal stress acting on the failure plane that forms in a deformed sample. The observed failure envelope is typically concave downward. This is true for rocks in general and for Westerly granite in particular [*Jaeger and Cook*, 1984; *Lockner*, 1995]. For simplicity, the Mohr-Coulomb linearized failure criterion

$$\tau = S_o + \mu_{\text{int}}\sigma_n \tag{1}$$

is often used to approximate the failure envelope [*Jaeger and Cook*, 1984, p100], where S_o is cohesion and $\mu_{\text{int}} = \tan\phi$ is coefficient of internal friction. In standard rock deformation experiments, τ and σ_n are not controlled or measured directly. In particular, the angle β that the eventual failure plane makes with the principal compressive stress axis (sample axis) is not

well constrained. It is found to vary by a few degrees between repeated experiments and in larger samples will often rotate during propagation of the fracture plane across the sample [*Lockner et al.*, 1992a]. The stresses measured directly in standard triaxial deformation experiments are confining pressure P_c ($= \sigma_2 = \sigma_3$) and axial stress σ_1 (all measured positive in compression). The experimental data shown in Figure 1 are replotted in Figure 2 with differential stress σ_Δ ($= \sigma_1 - P_c$) plotted versus P_c. Recall that shear and normal stresses on the fracture plane are obtained from

$$\tau = \frac{1}{2}\sigma_\Delta \sin(2\beta) \tag{2a}$$

$$\sigma_n = P_c + \frac{1}{2}\sigma_\Delta[1 - \cos(2\beta)] . \tag{2b}$$

A variety of empirical or semiempirical failure criteria such as (1) have been proposed (see *Lockner* [1995] for a brief summary). These generally include a nonlinear term to match the curvature of the observed failure envelope. In the present paper, however, we will present a more general constitutive expression for brittle rock which describes the overall stress-strain response of a sample and how it depends on strain rate, temperature, and confining pressure. Such a constitutive law should be able to predict failure envelopes as depicted in Figures 1 and 2.

In this paper we will not attempt to determine the full tensor coefficients relating stress, strain, and strain rate components. Instead, we will restrict ourselves to considering the interdependency of only the axial components of stress, strain, and strain rate. In the triaxial (axisymmetric) geometry, these are principal stress and strain components and represent maximum compressive stress and strain. A more generalized tensor relation may be developed at a later time. An important constraint of the axisymmetric test geometry is that the intermediate and minimum principal stresses are the same
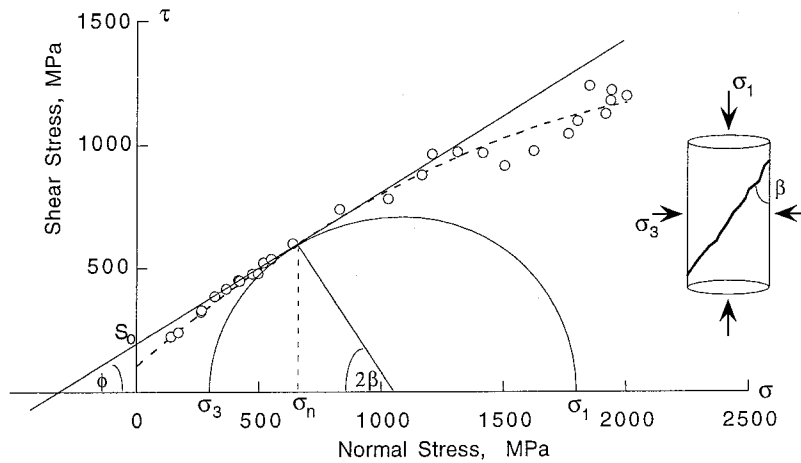
Figure 1. Mohr diagram for intact Westerly granite (data from *Byerlee* [1967]) showing the variation of shear strength as a function of normal stress on the eventual fracture plane. The failure envelope is characteristically concave downward, although it is often approximated by a Mohr-Coulomb linear failure criterion.

($\sigma_2 = \sigma_3 = P_c$). While a limited number of studies have been carried out on true triaxial machines, the effect that independent variation of σ_2 has on brittle fracture is not fully understood. We will show that in the axisymmetric case, the key constitutive law parameters can be described as simple functions of axial stress and confining pressure. When sufficient data become available to extend the model, we expect that the confining pressure dependence will be separable into functions of σ_2 and σ_3.

As a first step in this approach, we developed a constitutive law for creep in granite based on stress-stepping experiments carried out between 65 and 90% failure strength [*Lockner*, 1993b]. This law was based on reaction rate theory and linear fracture mechanics analysis of growth of idealized microcracks embedded in an elastic medium. The law related strain rate to stress and strain by considering corrosion reactions of water attacking Si-O bonds at the tips of growing microcracks. It had the general form

$$\dot{\varepsilon}_v = \dot{\varepsilon}_{vo} \exp\left(\frac{-[E^* - f(P_c, \sigma_\Delta, \varepsilon_v)]}{RT}\right) \qquad (3)$$

where, as listed in Table 1, ε_v and $\dot{\varepsilon}_v$ are inelastic volumetric strain and strain rate, $\dot{\varepsilon}_{vo}$ is a reference strain rate, E^* is apparent activation energy, R is the gas constant, and T is absolute temperature. The function $f(P_c, \sigma_\Delta, \varepsilon_v)$ modifies the activation energy and reflects the influence of applied stress and strain on the crack tip stresses. The model used analytic expressions developed by *Ashby and Hallam* [1986] which described how remote compressive stresses are converted to tensile stresses at crack tips of idealized microcracks. As derived by *Lockner* [1993b], the dependence of f on the remote stresses and volumetric strain can be expressed as: $f(P_c, \sigma_\Delta, \varepsilon_v) = f_1(\varepsilon_v)[f_2(\varepsilon_v)\sigma_\Delta - P_c]^2$. The derivation of (3) was based on an assumption of isolated, noninteracting cracks. This assumption appears valid for primary and secondary creep phases in a constant stress experiment, or for stresses up to approximately peak stress in a constant strain rate experiment [*Lockner et al.*, 1992b; *Lockner*, 1993a; *Reches and Lockner*, 1994; *Moore and Lockner*, 1995]. These studies have shown that fault nucleation involves a change from predominantly independent microcrack growth to a mode of cooperative growth that takes over once cumulative crack densities are high enough for microcracks to interact. This type of crack interaction was not considered by *Lockner* [1993b], and consequently, equation (3) was intended to describe transient or primary creep that occurs prior to fracture nucleation. We will include this transient creep response in our generalized constitutive equation.

Static fatigue is another phenomenon well known in rock mechanics and mining engineering [*Griggs*, 1939; *Mould and Southwick*, 1959; *Wiederhorn and Bolz*, 1970; *Scholz*, 1972; *Wawersik*, 1973; *Cruden*, 1974; *Kranz*, 1980; *Kranz et al.*, 1982; *Lockner and Madden*, 1991b; *Lockner*, 1993b]. It refers to the delayed failure of rock or other brittle material when
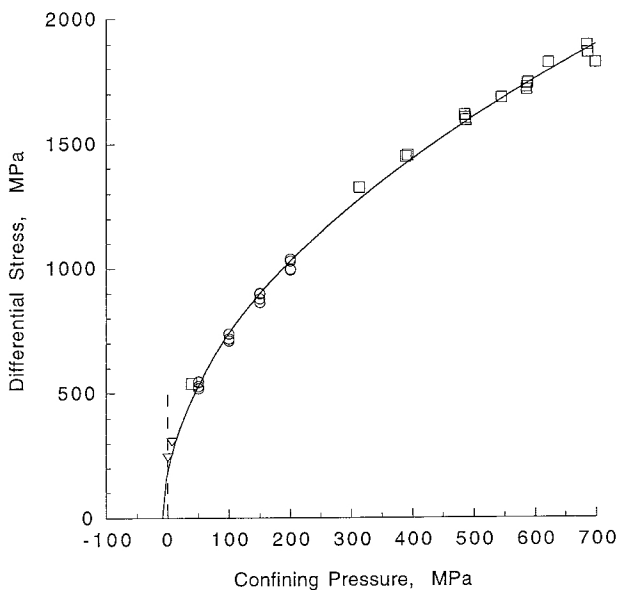

Figure 2. Failure envelope for Westerly granite plotting peak differential stress ($\sigma_{\Delta p}$) as a function of confining pressure. Data are squares from *Byerlee* [1967], triangles from *Wawersik* [1973], and circles from this study. Empirical quadratic fit of P_c versus $\sigma_{\Delta p}$ is also shown (equation (8)) which is more satisfactory that fitting $\sigma_{\Delta p}$ as a function of P_c.

Table 1. Mathematical Symbols

Symbol	Equation First Used	Definition
a	(11)	log strain rate sensitivity of stress before faulting
a_{fric}	(25)	log strain rate sensitivity of shear stress during frictional sliding
b_{fric}	(25)	state sensitivity of shear stress during frictional sliding
E^*	(3)	apparent activation energy
k	(23)	machine/rock stiffness
L	(23)	sample length
m	(12)	temperature dependence of a
P_c	(2)	confining pressure ($P_c = \sigma_2 = \sigma_3$ in triaxial test)
r	(5)	reaction rate
R	(3)	gas constant
S_o	(1)	cohesion
T	(3)	temperature
t_f	(4)	time to failure in constant stress test
u	(22)	axial displacement
V	(25)	sliding velocity on fault
v^*	(5)	apparent activation volume
α	(10)	arbitrary constant; shape factor for stress-strain relation at constant strain rate
β	(2)	angle between σ_1 and fault plane
ε_e	(22)	elastic strain
$\varepsilon_i, \dot{\varepsilon}_i$	(6)	inelastic axial strain, strain rate
ε_f	(A1)	inelastic strain when sample first attains frictional strength
ε_n	(A1)	inelastic strain at fault nucleation
$\varepsilon_v, \dot{\varepsilon}_v$	(3)	inelastic volumetric strain and strain rate
$\varepsilon_T, \dot{\varepsilon}_T$	(22)	total axial strain, strain rate
ε_o	(9)	inelastic strain at peak stress in constant strain rate test; function of P_c
$\dot{\varepsilon}_o$	(6)	reference state inelastic strain rate
φ	(10)	'strain angle' (see eq. 10)
μ	(A3)	τ / σ_n, coefficient of friction
μ_{int}	(1)	coefficient of internal friction
θ	(25)	state variable for frictional sliding on fault
$\sigma_1, \sigma_2, \sigma_3$	(2)	principal stresses
σ_n	(1)	normal stress
σ_{rs}	(5)	reaction site stress
σ_Δ	(2)	$\sigma_1 - P_c$, differential stress
$\sigma_{\Delta f}$	(A1)	differential stress for frictional sliding
$\sigma_{\Delta n}$	(A1)	differential stress at fault nucleation
$\sigma_{\Delta p}$	(11)	peak (or ultimate) differential stress in constant strain rate test
$\sigma_{\Delta po}$	(7)	peak differential stress at reference state ($\varepsilon_o, \dot{\varepsilon}_o, T_o$); function of P_c
τ	(1)	shear stress

and pressures below which dislocations and twinning are activated, then the nonlinear viscous response of a rock is primarily the result of microcrack growth and frictional sliding between grains [*Tapponnier and Brace*, 1976; *Lockner and Madden*, 1991a; *Savage et al.*, 1996]. In this case, the concept of subcritical crack growth [*Atkinson*, 1987; *Lockner*, 1993b] and the stress sensitivity of microcrack growth rate provide a mechanism for the observed stress dependence of inelastic strain rate in rock. The concepts of static fatigue and stress-sensitive deformation rate will also be incorporated into our generalized rheological model.

2. Rheological Model: Basic Form

In this section we present the basic form of the rheological model. Evaluation of empirical coefficients will be added in section 4, after presenting experimental data used in the empirical fits. We will use the same basic argument presented in our earlier creep study [*Lockner*, 1993b]. Namely, over a broad range of strain rates realizable in the laboratory (roughly 10^{-10} to 10^{-3} s^{-1}), brittle, inelastic deformation in rock is controlled by subcritical microcrack growth. Given the ample supporting evidence from thin section analysis and acoustic emission (AE) studies, this seems a reasonable starting point [*Scholz*, 1968a; *Peng and Johnson*, 1972; *Tapponnier and Brace*, 1976; *Kranz*, 1979, 1983; *Madden*, 1983; *Lockner and Madden*, 1991a,b; *Lockner et al.*, 1992a,b; *Lockner*, 1993b; *Moore and Lockner*, 1995]. Spontaneous high-frequency acoustic emissions are commonly associated with brittle rock deformation and indicate that microcracks are advancing fast enough to radiate acoustic energy. However, a comparison of total microcrack growth and cumulative AE suggests that <1% of microcracks generate detected AE [*Lockner*, 1993a]. Either detection levels are not sensitive enough to record most AE events, or most microcrack growth is aseismic with low propagation velocity. We have argued for the latter explanation, but observational evidence at this time is not conclusive.

We next assume that inelastic deformation will be represented by modification of the chemical reaction rate equation

$$\ln\left(\frac{r}{r_o}\right) = c - \left(\frac{E^* - v^* \sigma_{rs}}{RT}\right) \tag{5}$$

where r is reaction rate, c is a constant, and E^* and v^* are apparent activation energy and activation volume, respectively. Activation volume is more properly associated with pressure, rather than stress. Indeed, the precise dependence of Gibbs free energy on stress is still a matter of debate. It is an experimental fact, however, that crack growth rate is sensitive to crack tip stress [*Atkinson*, 1987]. We will treat the validity of (5) as an assumption of our model, pending resolution of the theoretical issues regarding the thermodynamic role of stress. Equation (5) states that an energetically favored reaction will progress at a rate determined by the rate of successful attempts to overcome an energy barrier represented by the activation energy. In addition, if the reaction sites are stressed, the effective energy barrier is reduced by an amount $v^* \sigma_{rs}$. An immediate consequence of (5) is that it implies an exponential relationship between driving stress and reaction rate (which is related to inelastic strain rate). This exponential relationship between stress and deformation rate is an ubiquitous feature of

loaded to a stress level less than the short-term failure stress. Time to failure t_f is found empirically to be related to stress either through exponential or power law forms [*Kranz*, 1980; *Lockner and Madden*, 1991b; *Lockner*, 1993b]. Consideration of reaction rate theory [*Scholz*, 1968a; *Lockner*, 1993b] leads to exponential stress dependence

$$t_f = t_o e^{-b\sigma} . \tag{4}$$

In this paper we will develop a model consistent with the exponential form.

The sensitivity of strain rate to applied stress level [*Wawersik*, 1973; *Lockner and Byerlee*, 1977; *Lockner and Byerlee*, 1980; *Lockner*, 1993b] is another manifestation of the processes leading to static fatigue. A feature common to polycrystalline rocks is that they exhibit a viscoelastic response when loaded to stresses above about half the failure stress. If we consider only brittle deformation, at temperatures

brittle deformation found for both intact rock deformation and for frictional sliding.

If brittle deformation is controlled by a characteristic stress corrosion reaction at microcrack tips and if this characteristic reaction is represented by equation (5), then two steps remain. First, because v^* and σ_{rs} represent conditions at the reaction sites, these parameters must be related to the remote boundary stress and displacement conditions applied to the sample. The overall compressive stresses applied at the boundaries are converted by local stress concentrators to tensile stresses which promote microcrack growth. In dense, crystalline rock, application of hydrostatic stress will tend to close cracks and to reduce crack tip tensional stresses. In porous sandstones, the reduced areas of contact where grains touch each other tend to act as stress concentrators even under hydrostatic loading. Consequently, grain crushing can occur under simple hydrostatic loading for some sandstones. Since we will be restricting our analysis to Westerly granite, a dense, crystalline rock, we expect that hydrostatic loading will tend to stabilize the sample and that deviatoric stress is necessary to promote microcrack growth. This effect has been modeled, for example by *Lockner and Madden* [1991a,b] and is consistent with the confining pressure dependence of the failure envelope shown in Figure 2.

The second step in the formulation requires the reaction rate r to be related to inelastic strain of the sample. In *Lockner* [1993b] we related crack tip stress to the remotely applied stress by using equations developed for idealized cracks embedded in an elastic medium [*Ashby and Hallam,* 1986]. We then integrated the effects of individual crack tip reactions to relate reaction rate to inelastic strain rate. We do not, however, have adequate theory to describe growth of interacting cracks which will dominate the final, important breakdown phase of sample deformation (although this has recently been investigated, for example, by *Okui and Horii* [1997]). Therefore, in the present exercise, we resort to an empirical fit of experimental data to build our rheological model. We use Westerly granite as a candidate rock type because it provides good reproducibility and because it has been studied extensively.

Our rheological model will be based on a modified rate equation of the form

$$\ln\left(\frac{\dot{\varepsilon}_i}{\dot{\varepsilon}_o}\right) = c_o - \frac{E^*}{RT} + f(P_c, \sigma_\Delta) g(\varepsilon_i) , \qquad (6)$$

where $\dot{\varepsilon}_i$ is inelastic axial strain rate, $\dot{\varepsilon}_o$ is a reference strain rate and, c_o is a constant to be determined. Functions $f(P_c, \sigma_\Delta)$ and $g(\varepsilon_i)$ will be empirically determined from triaxial experiments. These functions represent the dependence of reaction site stress on the applied boundary stress and inelastic axial strain. For noninteracting cracks, the influences of remote stress and strain appeared together in the rate equation as discussed after equation (3) above. As a working hypothesis, we adopt the same general form in (6) but do not consider that this form has been derived in any rigorous way. A more complete model would require parameters relating the complete tensor properties of stress and strain but is beyond the scope of the present analysis. Instead, we will build a rheological model which includes the fewest possible parameters and which can describe the available experimental data.

3. Experimental Procedure

A set of 16 constant strain rate experiments were conducted on room-dry samples of Westerly granite. Four experiments each were performed at confining pressures of 50, 100, 150, and 200 MPa. For each set of four runs, two were deformed at an axial shortening rate of 1 μm/s ($\dot{\varepsilon}_T = 1.57 \times 10^{-5}$ s^{-1}) and the two others at 0.01 μm s^{-1} (1.57×10^{-7} s^{-1}). In the slow experiments, initial loading to approximately one half of peak stress was carried out at 1 μm s^{-1} and then reduced to 0.01 μm s^{-1} for the remainder of the experiment. Samples were 25.4-mm-diameter right cylinders with length $L = 63.5$ mm and were all cored from the same starting block of granite to assure uniformity. Extra care was used in preparing identical, high-quality samples to improve reproducibility. Samples were jacketed in polyurethane tubing, pressurized and deformed at room temperature in a triaxial loading frame. Axial load and displacement were measured outside the pressure vessel. Measurement precision was axial displacement of ±0.2 μm (axial strain of ±3×10^{-6}); confining pressure of ±0.05 MPa; and axial stress of ±0.1 MPa. Pressure, axial stress and displacement were sampled every second in the fast experiments and every 2 in the slow experiments. Confining pressure was typically held constant to ±0.1 MPa during each experiment. Elastic stiffness of the loading frame plus sample was determined from the initial slope of the stress-displacement curves (Figure 3a) to be $k = 345 \pm 6$ MPa mm^{-1}.

4. Results

Stress-strain plots of four experiments conducted at 200 MPa confining pressure are shown in Figure 3a. Experiments run at the slower strain rate are ~4% weaker than the fast runs. This is characteristic of the strain rate dependence of strength [*Lockner*, 1995]. The same experiments are shown in Figure 3b with the elastic component of axial strain ($\varepsilon_e = \sigma_\Delta /(kL)$) removed so that the horizontal axis shows only the inelastic axial strain. The offset in the slow experiments at 700 MPa is the result of decreasing strain rate from 1 to 0.01 μm s^{-1} at this point. This was done to shorten the total length of these experiments so that the initial loading, which involves almost no inelastic deformation, is accomplished quickly. The characteristic shapes of the stress-strain curves shown in Figure 3b will be used to define the empirical functions $f(P_c, \sigma_\Delta)$ and $g(\varepsilon_i)$ that are used in the rheological model. Peak strengths $\sigma_{\Delta p}$ for the 16 experiments conducted are plotted in Figure 2 along with earlier measurements [*Byerlee*, 1967; *Wawersik*, 1973] for Westerly granite. A good fit to the observational data is given by

$$\sigma_{\Delta po} = -8.3 + (46{,}660.4 + 5128.7 P_c)^{\frac{1}{2}}$$

$$0 \leq P_c \leq 700 \text{MPa} \qquad (7)$$

and is also plotted in Figure 2. For the remainder of this paper we will make the distinction between $\sigma_{\Delta p}$ (peak strength at arbitrary values of temperature and strain rate) and $\sigma_{\Delta po}$ (peak strength at reference state values of temperature and strain rate, as defined in Table 2). Equation (7) is the inverse of the formula

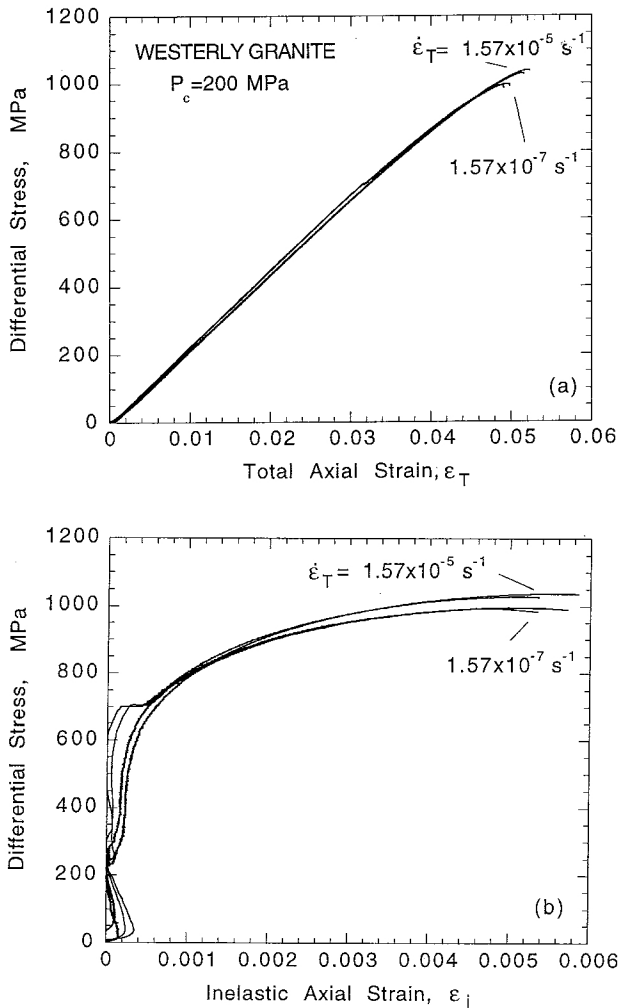$$P_c = 0.000195 \sigma_{\Delta po}^2 + 0.00324 \sigma_{\Delta po} - 9.08 \qquad (8)$$

Figure 3. (a) Stress-total strain plots for four experiments at P_c = 200 MPa. Faster experiments are about 4% stronger than slower experiments. (b) Same experiments plotting stress versus inelastic strain showing slight weakening prior to failure. Horizontal offset in slow experiments at 700 MPa stress is the result of reducing strain rate from fast to slow rate at this stress (see text). Little inelastic strain occurs below about 50% peak stress.

and is used in this paper to represent Westerly granite failure strength. We could have expressed $\sigma_{\Delta po}$ as a polynomial in P_c. However, (7) provides a better fit to the experimental data, especially in terms of matching both the values and slopes near the high and low limits.

4.1. Critical Strain

The notion of a characteristic or critical strain associated with sample failure has been proposed for brittle fracture [*Griggs*, 1940; *Scholz*, 1968b; *Cruden*, 1974; *Kranz and Scholz*, 1977; *Lockner*, 1993b]. From a damage mechanics view, critical strain would be associated with the cumulative damage needed for loss of structural integrity of the sample. *Madden* [1983] argued for a critical microcrack density needed for sample failure. We have confirmed the observations of the

accumulation of a critical crack density for fault nucleation in Westerly granite [*Lockner et al.*, 1992b; *Moore and Lockner*, 1995]. This critical crack density occurs when crack interaction dominates further crack growth and can be related to the ratio (crack spacing/crack length) [*Lockner et al.*, 1992b; *Reches and Lockner*, 1994; *Kuksenko et al.*, 1996]. Further discussion of critical strain appears in the appendix.

In Figure 3b the natural choice of a characteristic strain is inelastic strain at peak stress, denoted by ε_0. This parameter depends on confining pressure and is listed in Table 3 along with peak stress values. A linear fit of the form

$$\varepsilon_0 = c_1 + c_2 P_c \qquad (9)$$

gives $c_1 = 0.00121$ and $c_2 = 1.92 \times 10^{-5}$ MPa^{-1}. The strain data and a linear fit are plotted as a function of confining pressure in Figure 4. Our test samples consistently underwent a small amount of strain weakening, following peak stress, before fault formation. Thus, strain at peak stress, ε_0, is found to be ~90% of strain at fault nucleation ε_n. We will use ε_0 as a reference strain since it coincides with the reference stress state $\sigma_{\Delta po}$. In (9) we assume that ε_0 depends only on confining pressure. It may be temperature dependent, but we have no data to determine this. We do make the assertion that there is no significant strain rate dependence of ε_0. This assertion is consistent with the rather limited strain rate data available to us (2 orders of magnitude) and warrants further investigation. Implicit in (9) is an assumption that microcrack growth and the accompanying structural degradation of the rock is tied to the macroscopic strain field independent of strain rate.

4.2. Stress-Strain Relation

The rheological model will require an empirical fit to the stress-strain curves shown in Figure 3b. Even a fourth-order polynomial provides a poor fit to these curves. We seek a function that (1) matches the general shape of the observed curves, (2) has a steep slope at the origin, and (3) has a smooth and monotonically decreasing slope. We adopt a characteristic function of the form

$$\frac{\sigma_\Delta}{\sigma_{\Delta po}} = \sin^\alpha\left(\frac{\pi}{2}\frac{\varepsilon_i}{\varepsilon_0}\right) = \sin^\alpha(\varphi) = \frac{1}{g(\varepsilon_i)}$$

$$0 \le \frac{\varepsilon_i}{\varepsilon_0} \le 1.1 \qquad (10a)$$

with the definition

$$\varphi = \frac{\pi}{2}\frac{\varepsilon_i}{\varepsilon_0} \qquad (10b)$$

and arbitrary constant α. Thus a characteristic stress-strain curve is used to represent experimental data at all confining

Table 2. Reference State Values

Symbol	Definition
a_0	0.008 (*a* evaluated at $T = T_0$)
T_0	23°C (296.15°K)
ε_0	strain at peak stress (see equation (9))
$\dot{\varepsilon}_0$	1.57×10^{-5} s^{-1} (1 μm s^{-1} axial shortening rate)
$\sigma_{\Delta po}$	peak stress (see equation (7))

Table 3. Parameters Derived from Experiments

Sample	P_c, MPa	$\dot{\varepsilon}_T$ [†]	$\sigma_{\Delta p}$, MPa	ε_0, $\times 10^{-3}$	$\sigma_{\Delta po}$, average	a, $\times 10^{-3}$
w05-1	50	fast	543.2	1.75	544.5	8.81
w05-2	50	fast	545.9	1.99		
w05-3	50	slow	527.6	2.5		
w05-4	50	slow	518.3	2.19		
w10-1	100	fast	737.2	3.14	737.1	7.07
w10-2	100	fast	737.5	3.06		
w10-3	100	slow	709.2	3.68		
w10-4	100	slow	716.5	3.36		
w15-1	150	fast	899.2	3.59	898.1	6.84
w15-2	150	fast	897.1	3.96		
w15-3	150	slow	877.1	4.03		
w15-4	150	slow	862.6	3.93		
w20-1	200	fast	1028.4	5.12	1033.0	8.04
w20-2	200	fast	1037.6	5.56		
w20-3	200	slow	996.7	5.09		
w20-4	200	slow	993.3	4.72		

[†]Fast = 1.57×10^{-5} s^{-1}; slow = 1.57×10^{-7} s^{-1}.

pressures with differential stress and inelastic axial strain normalized by $\sigma_{\Delta p}$ and ε_0, respectively. Confining pressure dependence of these parameters is given by (7) and (9). The 1 μm s^{-1} strain rate experiments at 50, 100, 150, and 200 MPa confining pressure are plotted in Figure 5a along with a synthetic curve using (10) and $\alpha = 0.16$. This value of α will be used throughout this paper.

Equation (10) applies to deformation distributed throughout the sample; that is deformation leading up to strain localization and fault nucleation. In the appendix, we present data from 38.1-mm-diameter samples that suggest fracture nucleation initiates at a characteristic strain $\varepsilon_n \approx 1.1\varepsilon_0$. Once a fracture nucleates, the sample undergoes a rapid loss of strength which stabilizes at the frictional sliding strength. A representative strength curve is shown in Figure 5b. A discussion of the postnucleation phase is deferred to the appendix since the principal deformation characteristics dealt with in this paper are related to the prenucleation region represented by (10).

Figure 4. Plot of critical inelastic strain versus confining pressure. Linear fit is given by equation (9).

4.3. Strain Rate Dependence of Stress

We have shown (Figure 3b) that a two-decade decrease in strain rate results in an approximate four percent decrease in peak strength. To show this in more detail, we have subtracted the empirical strength curve (equation (7)) from peak strength data for 16 constant strain rate experiments. The residuals, plotted in Figure 6a, show a systematic weakening of samples deformed at the slow strain rate. We next define the rate sensitivity of peak stress as

$$a = \frac{1}{\sigma_{\Delta p}} \frac{\partial \sigma_{\Delta p}}{\partial \ln \dot{\varepsilon}_i} . \qquad (11)$$

The form of (11) is consistent with experimental observations for both deformation of intact rock [*Lockner*, 1993b] and deformation on preexisting fractures [*Dieterich*, 1981; *Blanpied et al.*, 1995; *Blanpied et al.*, 1998]. (For slip on fractures, a somewhat different definition is used: $a_{\mathrm{fric}} = (1/\sigma_n)(\partial \tau / \partial \ln V)$ with normal stress held constant.) In laboratory simulated fault studies, a_{fric} is only weakly dependent on normal stress [*Kilgore et al.*, 1993]. We find a similar result for intact rock (Figure 6b) where a is plotted as a function of confining pressure. Results are also listed in Table 3. Numerical inversions of laboratory data [*Blanpied et al.*, 1998] yield $a_{\mathrm{fric}} = 0.006$ ± 0.003 for dry, room temperature granite friction experiments, a range of values that is in close agreement with the intact granite values ($a = 0.008 \pm 0.001$) reported here. (As shown in the appendix, a small scaling factor is required to convert from values of a evaluated parallel to the σ_1 axis and a_{fric}, which is evaluated on an inclined fault plane.) The micromechanical deformation mechanisms that control the response of a fault surface to a sudden change in slip rate are likely to be subcritical crack growth and contact interlocking. Since these same mechanisms are occurring during deformation of intact samples [*Savage et al.*, 1996], it is not surprising that the deformation rate sensitivity for intact rock and slip on fault surfaces should be similar.

While we have determined the value of a at room temperature, we have not conducted experiments to determine how a varies with temperature. Determinations of a_{fric} have been re-
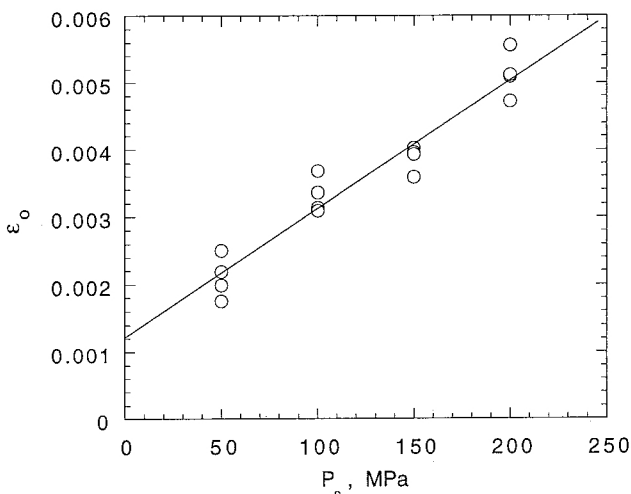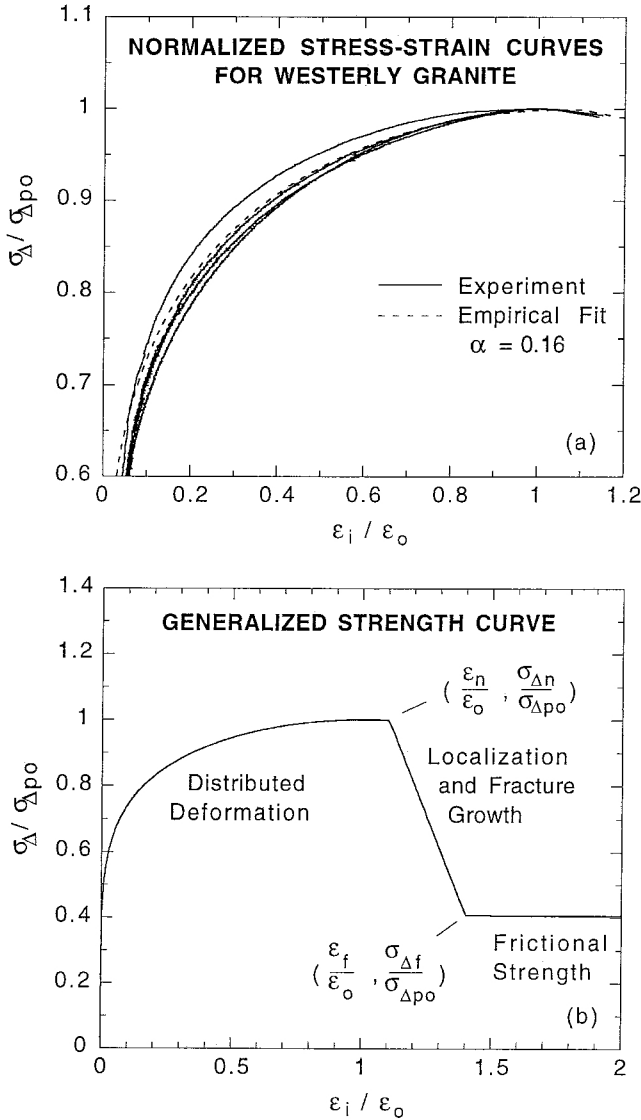
Figure 5. (a) Normalized stress versus strain (normalized by critical strain) for fast experiments at confining pressures of 50, 100, 150, and 200 MPa. Characteristic curve (equation (10)) is shown as dashed line and is used to represent stress-strain relation at all confining pressures. (b) Generalized stress/strain curve showing three stages of deformation. Distributed deformation with strain dependence given by equation (17) is followed by strain localization and fracture formation characterized by rapid strength loss (see the appendix). Final stage is frictional sliding on fully developed fault.

ported for dry granite gouge-filled fractures to 845°C [*Lockner et al.*, 1986] and wet granite gouge to 600° [*Blanpied et al.*, 1998]. Below 250°C, temperature dependence of a_{fric} is small and even the sign is not certain. Alternatively, we have evaluated subcritical crack growth data for tensile crack growth in Westerly granite [*Atkinson and Meredith*, 1987, Figure 4.9]. In this case, we find that the stress intensity factor tends to decrease with temperature: $\partial K_I / \partial T \cong -(7 \pm 2) \times 10^{-5}$ MPam$^{1/2}$ °K^{-1}. If this mechanism is responsible for the temperature dependence of a, we estimate $\partial a / \partial T \approx -3 \times 10^{-5}$ °K^{-1}. We will assume a functional form

$$a = a_o + m(T - T_o) \qquad (12)$$

where T_o is a reference temperature, although alternative forms are certainly possible.

5. Generalized Rheological Model

We now have all the necessary information to construct our generalized rheological model. We begin with (6), adopting the following functional forms for the dependence of reaction site stress on remotely applied stress and strain:

$$f(P_c, \sigma_\Delta) = \frac{\sigma_\Delta}{a \sigma_{\Delta po}} \qquad (13)$$

$$g(\varepsilon_i) = \sin^{-\alpha}(\varphi) \qquad (14)$$

where confining pressure dependence is given by (7) and (9) and φ is defined in (10b). Substitution into (6) gives

$$\ln\left(\frac{\dot{\varepsilon}_i}{\dot{\varepsilon}_o}\right) = c_o - \frac{E^*}{RT} + \frac{1}{a}\frac{\sigma_\Delta}{\sigma_{\Delta po}}\sin^{-\alpha}(\varphi)$$
$$0 \le \frac{\varepsilon_i}{\varepsilon_o} \le 1.1 \qquad (15)$$

We have set an upper strain limit for applicability of (15) of $\varepsilon_i = 1.1\varepsilon_o$ which, as we discuss in the appendix, represents the critical strain at which fracture nucleation occurs. The constant c_o can be determined by evaluating (15) at the reference state listed in Table 2. We find that $c_o = (E^*/RT_o) - 1/a_o$. The resulting rheological model then becomes

$$\ln\left(\frac{\dot{\varepsilon}_i}{\dot{\varepsilon}_o}\right) = \frac{E^*}{RT_o} - \frac{E^*}{RT} - \frac{1}{a_o} + \frac{1}{a}\frac{\sigma_\Delta}{\sigma_{\Delta po}}\sin^{-\alpha}(\varphi)$$
$$0 \le \frac{\varepsilon_i}{\varepsilon_o} \le 1.1 \qquad (16)$$

or, upon rearranging terms

$$\sigma_\Delta = \sigma_{\Delta po} a \sin^\alpha(\varphi)\left[\frac{1}{a_o} + \frac{E^*}{R}\left(\frac{1}{T} - \frac{1}{T_o}\right) + \ln\left(\frac{\dot{\varepsilon}_i}{\dot{\varepsilon}_o}\right)\right]. \qquad (17)$$

6. Discussion

When evaluated at room temperature ($T = T_o$, $a = a_o$), equation (17) reduces to

$$\sigma_\Delta = \sigma_{\Delta po} \sin^\alpha(\varphi)\left[1 + a_o \ln\left(\frac{\dot{\varepsilon}_i}{\dot{\varepsilon}_o}\right)\right] \qquad (18)$$

As required, we have recovered the simple functional form (10) with a log strain rate sensitivity of stress given by a_o. The full strain rate sensitivity is

$$\frac{\partial \sigma_\Delta}{\partial \ln \dot{\varepsilon}_i} = a \sigma_{\Delta po} \sin^\alpha(\varphi) \qquad (19)$$

so that at peak stress ($\varphi = \pi/2$) we recover equation (11).

6.1. Temperature Dependence

Temperature dependence of stress is determined from (17) as

$$\frac{1}{\sigma_{\Delta po}}\frac{\partial \sigma_\Delta}{\partial(1/T)} = a\frac{E^*}{R}\sin^\alpha(\varphi) + \frac{1}{a}\frac{\sigma_\Delta}{\sigma_{\Delta po}}\frac{\partial a}{\partial(1/T)} \qquad (20)$$
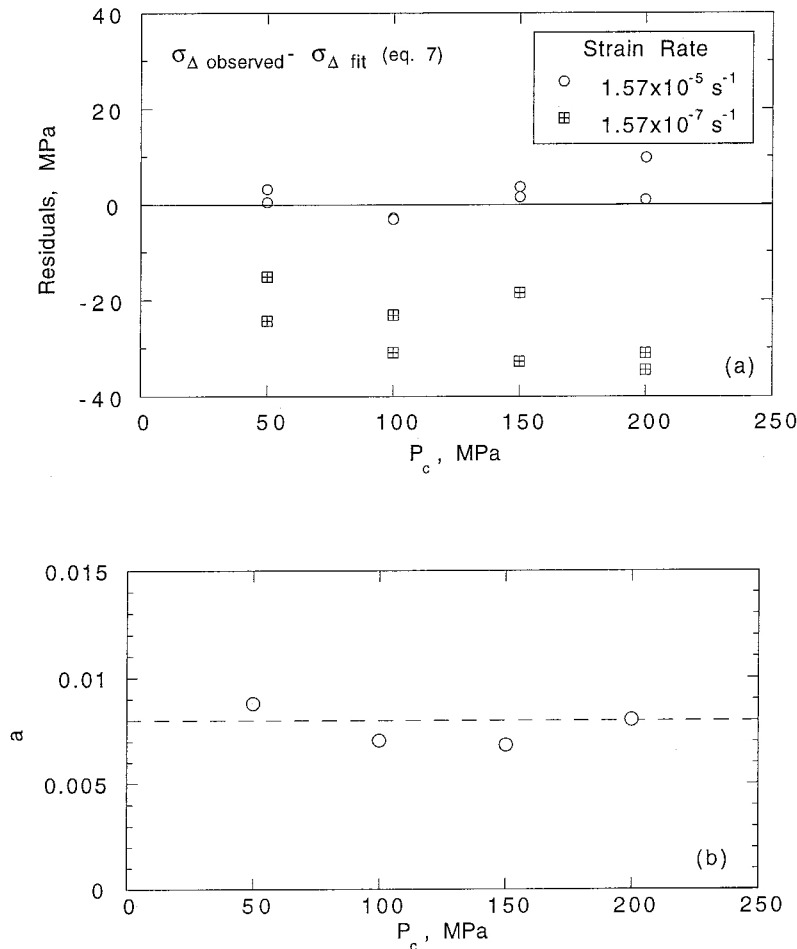
Figure 6. (a) Difference between observed peak strength $\sigma_{\Delta p}$ and least squares fit to strength under 'standard state' conditions (equation (7)) for fast and slow experiments. Slow experiments are systematically weaker due to strain rate sensitivity of stress as expressed by parameter a. (b) Strain rate sensitivity of stress plotted as a function of confining pressure showing little pressure sensitivity.

The first term on the right-hand side of equation (20) relates the Arhenius type interdependency of stress, temperature, and activation energy. The second term describes the effect of temperature-dependent variations in a on stress. If we assume a dependence of a on temperature as in equation (12), we find that $\partial a/\partial(1/T) = -mT^2$ and (20) becomes

$$\frac{1}{\sigma_{\Delta po}}\frac{\partial \sigma_\Delta}{\partial\left(\frac{1}{T}\right)} = a\frac{E^*}{R}\sin^\alpha(\varphi) - \frac{m}{a}\frac{\sigma_\Delta}{\sigma_{\Delta po}}T^2 \qquad (21)$$

If $|m| < a^2 E^*/(RT^2)$, the first term on the right-hand side of (21) dominates and a plot of normalized peak stress versus $1/T$ should result in a slope of a_oE^*/R. Proper experimental data for testing this relationship are not available. Temperature-stepping experiments carried out at constant strain rate would provide such a test. However, we have not conducted these measurements. For now, we show peak strength data from nominally dry deformation experiments of Westerly granite in Figure 7. Changes in microstructure due to thermally induced microcracks, as well as pressure sensitivity of crack growth can affect these peak strength data in a manner unaccounted for in the present model. Above about 300°C, dislocation creep mechanisms become increasingly important in lowering

strength and the present analysis will not be applicable. Below 300°C, however, we find an average slope of 74 ±42°K, which implies an apparent activation energy of $E^* = 77$ ±43 kJ mol^{-1}. Values reported for single crystal quartz [*Scholz,* 1972] and sandstone [*Rutter and Mainprice,* 1978] range from 83 to 100 kJ mol^{-1}. Substituting this activation energy into the above inequality requires, at 100°C, $|m| < 6\times10^{-5}$ /°K. Our rough estimate of m from mode I subcritical crack data, in the discussion preceding equation (12), is only marginally smaller than this restriction. Including $m = -3\times10^{-5}$ °K^{-1} in the above calculation does not significantly change the estimate of E^*. Still, the currently available experimental data are of insufficient accuracy to determine either E^* or m with confidence.

6.2. Numerical Modeling

In sections 6.3 through 6.5 we will compare the response predicted by the rheological model to a variety of constant stress and constant strain rate experiments. To facilitate this comparison, we have developed a simple forward time stepping numerical model based on (17) and incorporating elastic stiffness of the loading frame. Because of the wide range of possible strain rates (spanning over 10 orders of magnitude),
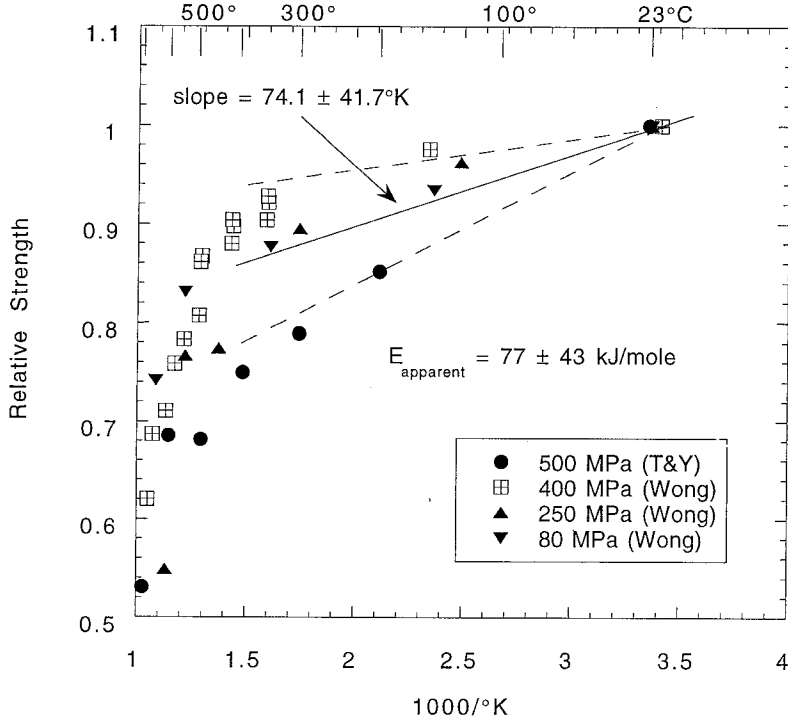
Figure 7. Relative strength of dry Westerly granite plotted as a function of inverse temperature. Data from *Tullis and Yund* [1977] and *Wong* [1982]. Slope of temperature sensitivity for temperature below 300°C suggests apparent activation energy of 77 kJ mol^{-1}. Above this temperature, dislocation mechanisms are activated, and samples have moved into a different deformation regime.

the numerical model computes a variable time step based on predetermined maximum allowable changes in stress and strain. For convenience, we will restrict ourselves to modeling deformation experiments at room temperature.

Axial deformation u is measured at a fixed position outside the pressure vessel during each experiment. We express axial deformation in terms of an equivalent total strain $\varepsilon_T = u/L$ where L is sample length. Total strain is partitioned into two parts: elastic strain ε_e and inelastic strain ε_i, such that

$$\varepsilon_T = \varepsilon_e + \varepsilon_i \ . \tag{22}$$

Elastic strain is related to axial stress through the combined stiffness of the sample and loading frame

$$\sigma_\Delta = kL\varepsilon_e \tag{23}$$

where $1/k = 1/k_{\text{frame}} + 1/k_{\text{sample}}$. Initial slopes of stress-strain curves (Figure 3a) give $k = 345 \pm 6$ MPa mm^{-1}. Equation (18) can be rearranged to provide an explicit expression for inelastic strain rate in terms of inelastic strain and an applied stress boundary condition

$$\ln \dot{\varepsilon}_i = \ln \dot{\varepsilon}_0 + \frac{1}{a_0}\left[\frac{\sigma_\Delta}{\sigma_{\Delta po}}\sin^{-\alpha}(\varphi) - 1 \right] \tag{24a}$$

Alternatively, stress can be eliminated by combining (22) and (23) to give inelastic strain rate as a function of inelastic strain and a total strain boundary condition

$$\ln \dot{\varepsilon}_i = \ln \dot{\varepsilon}_0 + \frac{1}{a_0}\left[\frac{kL(\varepsilon_T - \varepsilon_i)}{\sigma_{\Delta po}}\sin^{-\alpha}(\varphi) - 1 \right] \tag{24b}$$

Finally, we note that for a fixed displacement boundary condition, the sample-loading frame system will become unstable (accelerating inelastic strain) when the unloading slope of the sample $(\partial\sigma_\Delta/\partial\varepsilon_i)$ exceeds the elastic unloading of the system $(-kL)$. As discussed in the appendix, rapid weakening is associated with fault nucleation and growth, beginning at $\varepsilon_n \approx 1.1\varepsilon_0$. Since we do not consider inertial effects in our computations, we stop deformation calculations when strain rate exceeds approximately 1 s^{-1} (63.5 mm s^{-1}).

6.3. Constant Strain Rate Simulations

The first series of simulations are at constant strain rate and constant confining pressure. Figure 8a plots stress versus total strain for three experiments at a strain rate of 1.57×10^{-5} s^{-1} along with the corresponding simulations. Owing to the relatively small amount of net inelastic shortening, these plots are generally dominated by elastic loading. Figure 8b shows the same experiments with only the inelastic strain component plotted. One well-documented feature of Figure 8b is that there is little appreciable inelastic strain below ~50% of peak strength. In general, the samples undergo a small amount of stable unloading following peak stress. This phase progresses into dynamic unloading of the system and violent stress drop represented by the straight-line segments of the curves after inelastic strains of 0.003 to 0.005. The slope of this dynamic unloading is controlled by the stiffness of the sample-loading frame system. A second series of experiments is plotted in Figure 9. In this case, axial shortening began at 1.57×10^{-5} s^{-1} and then was reduced at about half of the peak stress to 1.57×10^{-7} s^{-1}. The reduction in strain rate results in a horizon-
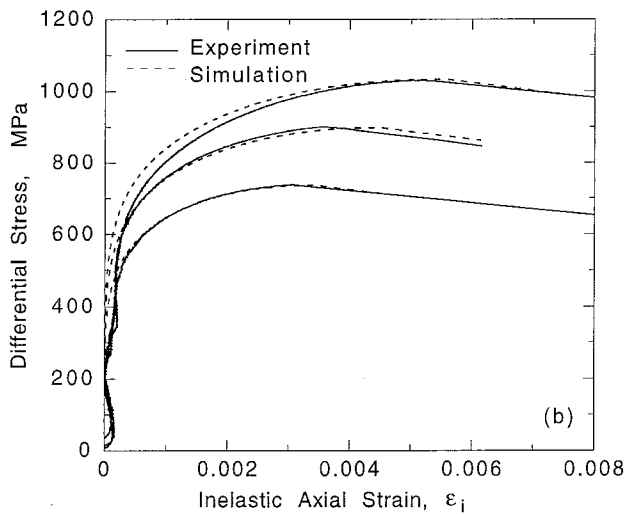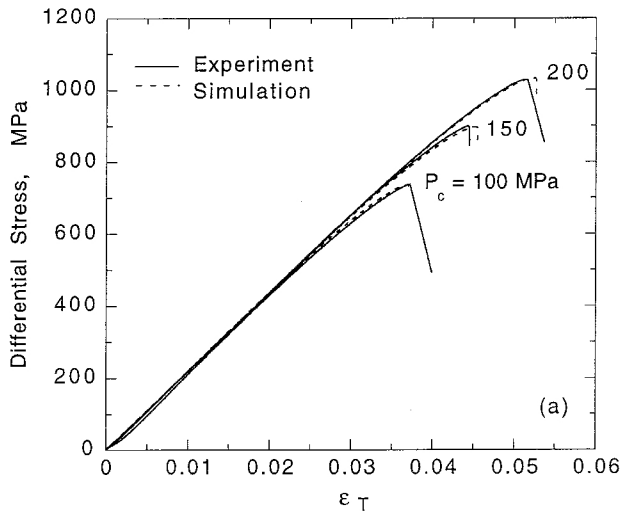
sents a lifetime of over 30 Myr. In each of the three creep experiments shown in Figure 10a, failure is delayed as inelastic strain (damage) accumulates in the sample. Finally, when enough damage has occurred to lead to fault nucleation, the stress-strain curves intersect the descending failure envelope and the sample fails. This process has been discussed by *Wawersik and Fairhurst* [1970] and *Lockner et al.* [1992b]. The same simulations are shown in Figure 10b with the elastic strain removed. Finally, strain is plotted versus time in Figure 10c for one of the simulations, showing the three characteristic creep phases: (1) primary or transient creep characterized by $\dot{\varepsilon}_i$ proportional to $1/t$; (2) secondary creep with nearly constant strain rate; and (3) accelerating or tertiary creep culminating in failure [*Lockner and Byerlee*, 1980; *Lockner and Madden*, 1991b; *Lockner*, 1993b]. The $1/t$ primary creep response is built into the rheological model since constant strain rate curves are spaced by $\ln \dot{\varepsilon}_i$. Secondary creep occurs in the transition region between decaying primary creep as noninteracting cracks strain harden and accelerating tertiary creep characterized by the gradual increase in crack interaction and
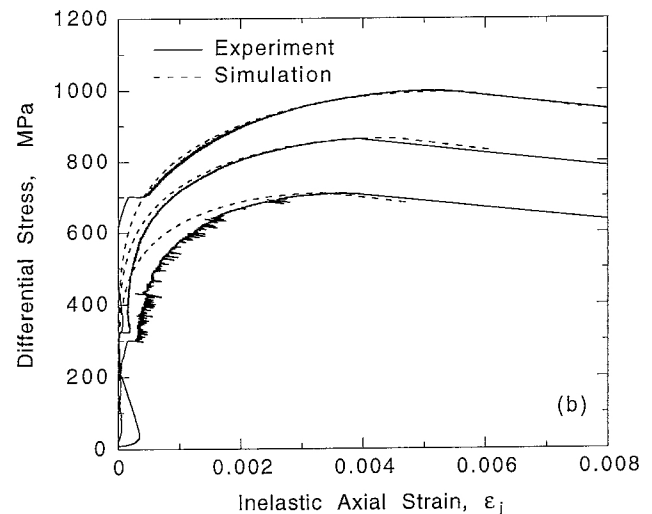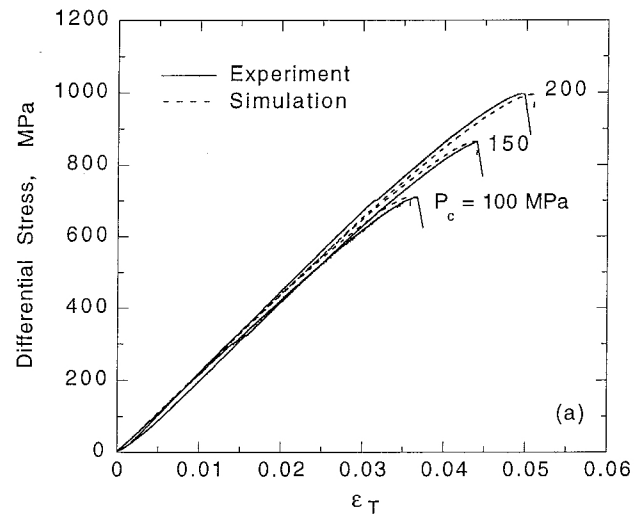
Figure 8. (a) Fast strain rate experiments (solid lines) at 100, 150, and 200 MPa confining pressure. Numerical simulations are shown as dashed lines. (b) Same experiments and simulations plotting stress versus inelastic strain. Postfailure slopes are controlled by machine stiffness. Peak stress, critical strain, and overall shape of stress-strain response are well-represented by rheological model.

tal jog in the stress-strain curve at about 300 and 700 MPa stress. While the simulations also contain this offset, they appear to underestimate the magnitude of the inelastic strain step. In other regards, the simulations do a good job of reproducing the observed strain behavior.

6.4. Constant Stress and Time to Failure

The next simulations (Figure 10) are three creep or constant stress experiments at 200 MPa confining pressure. In this case, simulations are ended when creep rate increases to 0.1 s^{-1}. Also plotted for reference are constant strain rate simulations at 10^{-4} and 10^{-18} s^{-1}. The fast strain rate experiment provides a reference failure envelope for rapid deformation; failure occurred after 5.5 min. The slow strain rate is intended to enclose a region in stress-strain space in which the rock is essentially stable. For example, if a sample can sustain inelastic strain in excess of 0.001 without failing, a strain rate of 10^{-18} s^{-1} repre-

Figure 9. (a) Slow strain rate experiments under conditions similar to, but weaker than, those of Figure 8. (b) Same experiments and simulations as in Figure 9a with stress plotted versus inelastic strain. Horizontal jog at low strain is result of a 2 decade drop in strain rate.
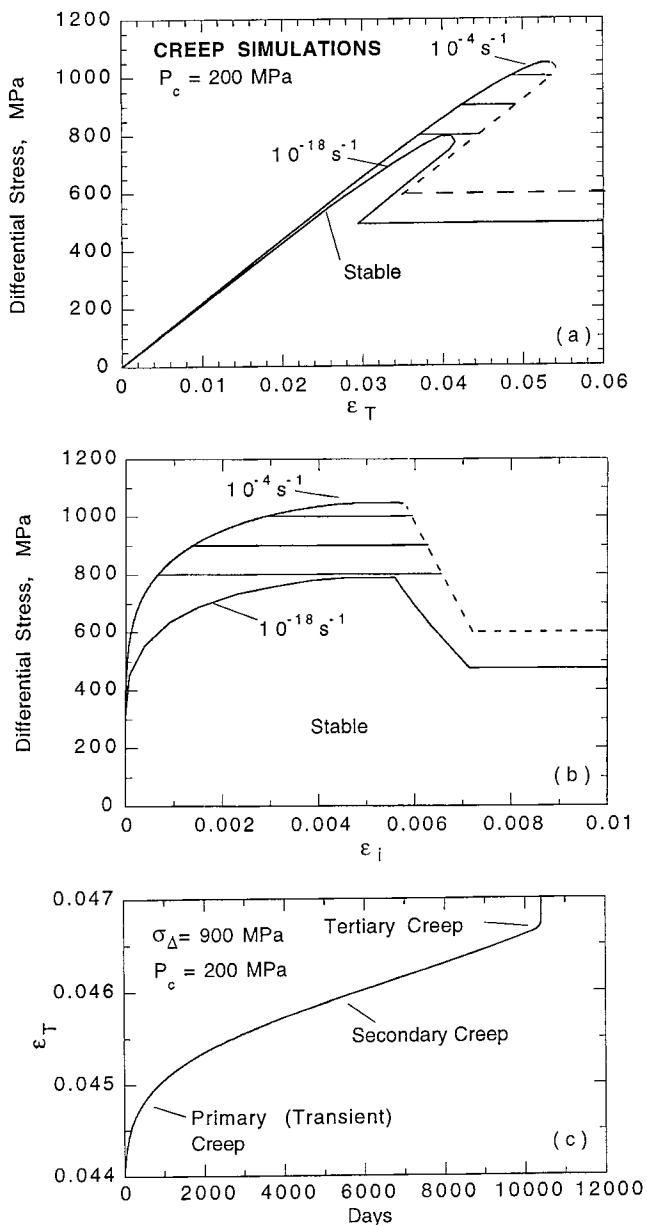
Figure 10. (a) Constant stress (creep) simulations at 800, 900, and 1000 MPa differential stress and 200 MPa confining pressure. Constant strain rate simulations at 10^{-4} and 10^{-18} s^{-1} are plotted for reference. During creep experiments, microcracks gradually grow by subcritical crack growth [*Lockner*, 1993b] until fault nucleation occurs. (b) Same simulations as in Figure 10a with stress plotted versus inelastic strain. Area under each curve represents irreversible work expended during creep. (c) Time plot of strain for 900 MPa creep simulation. Simulation exhibits three classic stages of creep [*Lockner and Byerlee*, 1980; *Lockner and Madden*, 1991b; *Lockner*, 1993b].

cooperative deformation. In this sense, secondary creep does not represent any unique process but rather a region in which two processes are nearly in balance. Tertiary creep represents the region of increasing crack interaction which culminates in fracture nucleation and failure.

Another set of three simulations were computed at constant total strain boundary conditions (Figure 11). By fixing total

strain, stress decreases monotonically as stored elastic energy is consumed by microcrack growth in the sample. As in the case of constant stress runs, if the initial stress level is low enough, the strain rate will drop to very low levels and the sample is stable over even geologic timescales. Of course, extrapolation from laboratory strain rates (greater than about 10^{-10} s^{-1}) to geologic timescales is uncertain since alternate deformation mechanisms such as pressure solution may become significant. Figure 11c plots the inelastic strain history for the simulation run at a total strain of 0.048. Even though stress is continuously decreasing during this simulation, the
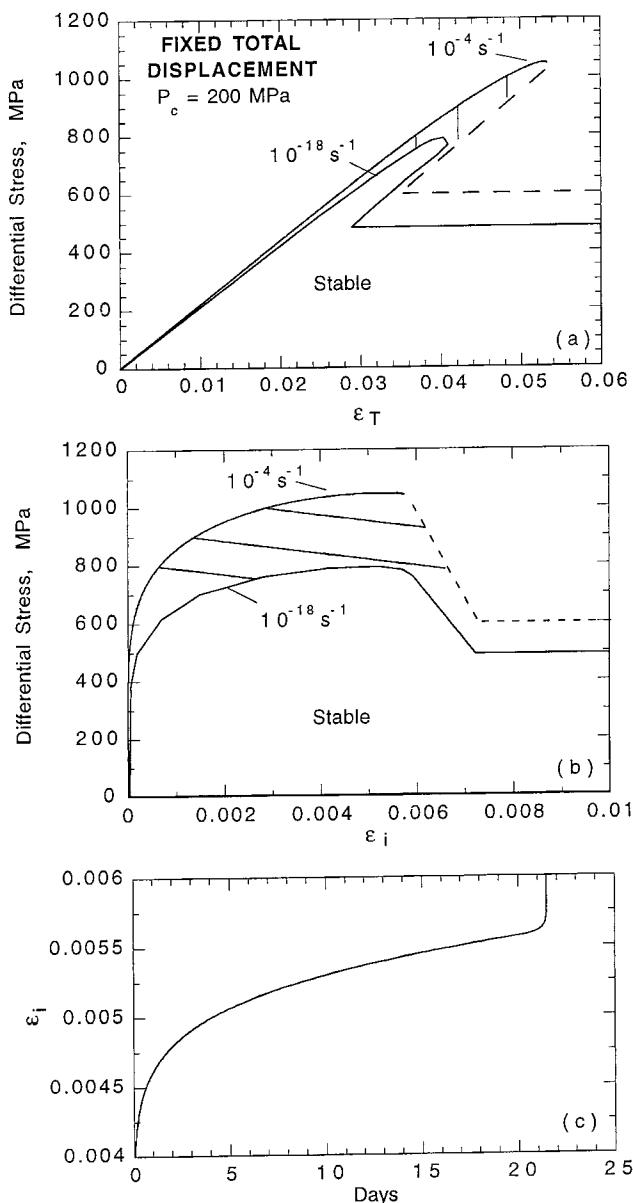

Figure 11. (a) Three simulations at constant total strain in which stored elastic energy is used to grow microcracks. (b) Stress versus inelastic strain showing gradual unloading at a rate controlled by machine plus sample stiffness. Simulation at 800 MPa intersects stable region of stress-strain space and never progresses to failure. (c) Inelastic strain history for simulation at 0.048 total strain. Similar to the creep simulations, this run shows three creep phases culminating in failure.
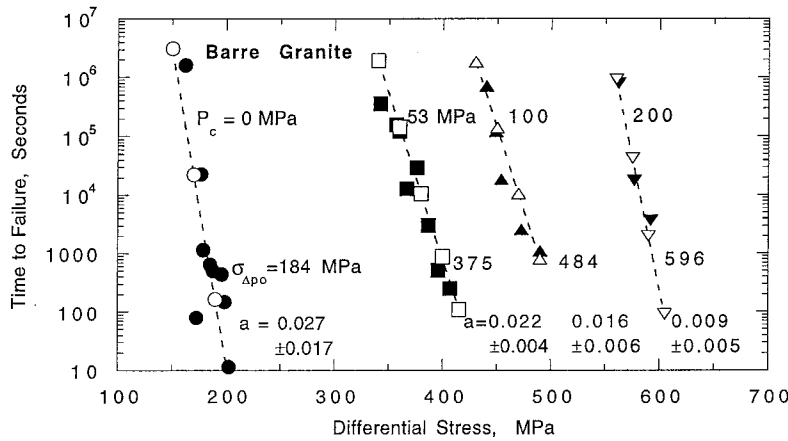
Figure 12. Time to failure plotted versus stress for Barre granite at four confining pressures (data from *Kranz* [1980]). Rate sensitivity a is selected to match experimental data and varies systematically with confining pressure. Note that exponential stress dependence is properly predicted by the rheological model.

strain history shows the same three creep phases observed in the constant stress experiments. This is not surprising when stress trajectories in Figures 10b and 11b are compared. While stress does decrease with strain in the simulations in Figure 11b, the decrease is relatively minor and not very different from the constant stress trajectories from the creep experiments. The main effect is to gradually drop to lower strain rates and therefore extend the timescale over which the deformation occurs.

Creep simulations like the ones shown in Figure 10 can be used to compute time to failure (t_f) response for granite loaded to some fraction of its short term failure strength. Good experimental data exist for Barre granite [*Kranz*, 1980] which is coarser grained and weaker than Westerly. Kranz's [1980] results are reproduced in Figure 12 along with simulations using his peak strength values (shown in Figure 12) and critical strain values. Average strain rate is just ε_n/t_f. Then, equation (11) suggests that the slope of the $\log t_f$ versus σ_Δ plot should be approximately $-1/(2.303 a_o \sigma_{\Delta po})$. We have adjusted a_o to match the observed trends in the Kranz data. Values of a_o that fit the experimental data are shown in Figure 12. For Westerly granite, a_o was found to be nearly independent of confining pressure (Figure 6b). By contrast, the Barre granite time to failure data suggest that a_o decreases with increasing confining pressure. However, given the uncertainty in the slope determinations, this has not been demonstrated conclusively. For example, the 200 MPa determination of a_o is sensitive to a single observation at $t_f = 10^6$ s. Moisture content in the samples is known to have an important influence on subcritical crack growth rates in tension [*Atkinson*, 1987] and needs to be controlled more carefully. It is probably better to carry out these experiments under fully saturated conditions to minimize the influence of variations in partial water saturation. What is clear from Figure 12 is that the exponential dependence of time to failure on applied stress is successfully reproduced by the rheological model as developed here. This relationship was pointed out by *Lockner* [1993b], who related the slope $(\Delta t_f/\Delta \sigma_\Delta)$ to the apparent activation volume associated with microcrack growth. This quantity is related to $a_o \sigma_{\Delta po}$ in the present formulation.

6.5. Strain Rate Stepping Experiment

As a final test of the rheological model, a deformation experiment was conducted at 50 MPa confining pressure and room temperature on a larger (76.2 mm diameter by 190.5 mm length) sample. In this case, axial stress was measured with an internal load cell so that variations in seal friction on the loading piston do not affect the stress measurements. A rock plus loading frame stiffness of $k = 129$ MPa mm^{-1} was determined from the stress-displacement curve. The sample was loaded by a sequence of constant strain rate steps, allowing stress to vary in response as shown in Figure 13a. Also plotted is the stress response in a numerical simulation which used the same strain rate boundary condition. Peak differential stress was 584 MPa which is ~7% above the peak value of the smaller samples used to determine model parameters in this paper. It is likely that this sample was cored from a different granite block than the 16 small samples reported on above. We have observed similar variations in strength of Westerly granite when blocks from different parts of the quarry were compared. Consequently, we used a larger value for the peak strength in modeling this experiment. Results from a simulation using $\sigma_{\Delta po} = 595$ MPa are shown as dashed lines in Figure 13a. Inelastic strain at failure is sensitive to the value used for characteristic peak strain (ε_o). The value used in this simulation (0.00245) is within the range of values determined from small sample calibration runs (Table 3). Other coefficients used in the simulation are the values determined from the 16 small sample calibration runs. During the real experiment, stress rose in steps in response to the varying strain rate history. Inelastic strain rate, computed by subtracting elastic strain rate from total strain rate, is also seen to respond to the rising stress level. While $\sigma_{\Delta po}$ was chosen to match the peak stress in the experiment, inelastic strain at failure could also be matched by choosing ε_o to be within the range observed in small samples experiments. Thus the small samples can be used to predict response of samples 3 times larger and tested in a loading frame having significantly different loading characteristics.

Detailed stress response to one of the strain rate sequences involving three decade steps in strain rate is shown in Figure
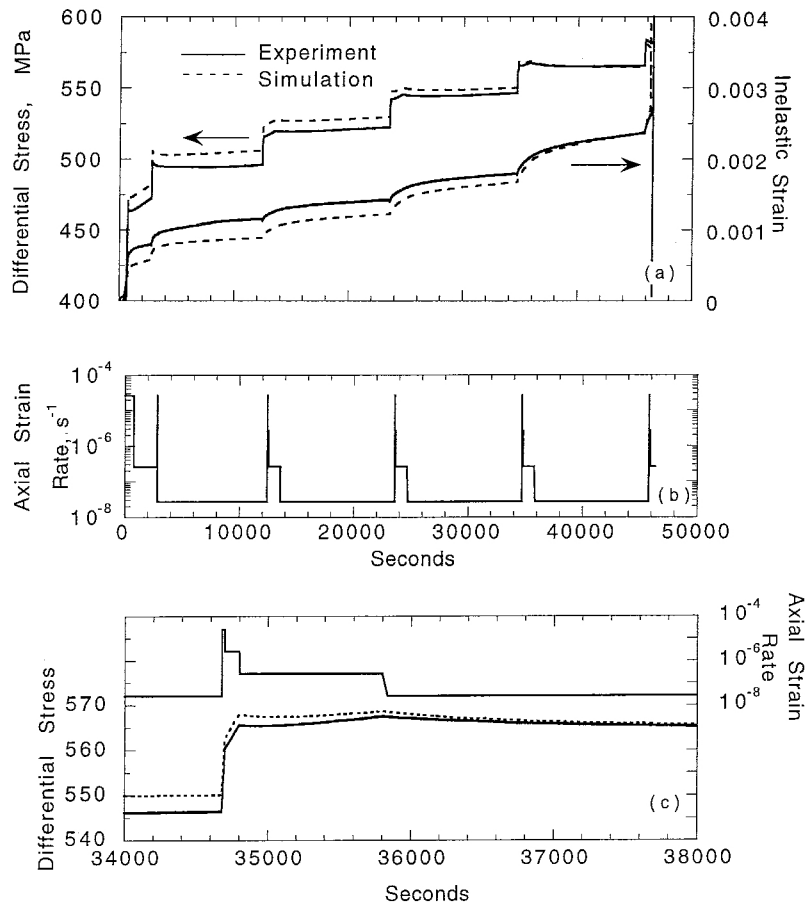
Figure 13. Strain rate stepping experiment conducted on 76.2 mm diameter dry Westerly granite sample at 50 MPa confining pressure. (a) Observed stress and inelastic strain response (solid lines) and numerical simulation (dashed lines). (b) Applied strain rate history. (c) Expanded view of one strain rate stepping sequence showing elastic response to two fastest strain rate steps but creep response to slower strain rate steps. Simulation captures all the significant features of the strain rate stepping sequence.

13c. The two fastest strain rate steps resulted in essentially elastic response of the sample. The next slower step at 34,800 s resulted in a shallow bay in stress followed by a gradual stress increase. The final slowest strain rate step at 35,800 s resulted in a slow but steady weakening of the sample. All of these features are accurately reproduced in the numerical simulation shown as the dashed line in Figure 13c.

6.6. Comparison to Frictional Sliding

We have noted the general form of the intact rock rheological model (18) bears a close resemblance to rate- and state-dependent constitutive laws developed to describe frictional sliding of Coulomb materials [*Dieterich*, 1981; *Kilgore et al.*, 1993; *Blanpied et al.*, 1998]

$$\tau = \tau_0 + a_{fric}\sigma_n \ln\left(\frac{V}{V_0}\right) + b_{fric}\sigma_n \ln\left(\frac{\theta}{\theta_0}\right) \qquad (25)$$

where θ is a state variable describing evolution of the fault material. We can evaluate intact rock strength near peak stress ($\varphi = \pi/2$), taking a series expansion of the inelastic strain dependence ($g(\varepsilon_i)$) and discarding terms of order $(\varepsilon_i - \varepsilon_0)^2$ and higher. Equation (18) then reduces to

$$\sigma_\Delta = \sigma_{\Delta po} + a_0\sigma_{\Delta po} \ln\left(\frac{\dot{\varepsilon}_i}{\dot{\varepsilon}_0}\right). \qquad (26)$$

A comparison of (25) and (26) shows the two constitutive laws have the same form with the exception that there is no evolution term in the intact rock relation. The evolution term is included in the frictional law to account for growth and decay of contacts resulting from finite slip on the fracture surface. Therefore it is not surprising that intact rock deformation, which results from the growth and collapse of distributed microcracks involving little net strain, should not require such a term. In fact, we anticipate that the functional form of (25) can be recovered from (26) by integrating over a population of contacts that are all in different stages of their growth/collapse sequences.

The a terms in (25) and (26) provide an immediate change in stress due to a change in strain rate. This is sometimes referred to as the instantaneous response. Strain would be concentrated in a narrow fault zone, so that relative displacements and movement of grains would be much greater than in distributed bulk deformation. Even so, this effect should only be applicable to the state variable b term since, at least in a mathematical sense, the instantaneous response does not require finite

displacement. The actual strain required for the 'instantaneous' response to occur is likely to be of the order of $\Delta\tau/G$, where G is the shear modulus of the contact resisting deformation.

7. Conclusions

In this paper we have developed an empirical constitutive law relating stress, strain and strain rate for deformation of Westerly granite based on an Arrhenius type reaction rate equation. The model assumes that inelastic deformation within the rock is the result of microcrack growth which is thermally activated and which can be related to boundary stresses and strains through characteristic functions. Consequently, inelastic strain rate can be related to applied stress, strain, and temperature according to equation (16). At room temperature, this relation simplifies to equation (18). This equation applies to distributed deformation prior to fault nucleation. Fault formation and frictional sliding stages are considered in the appendix. Application of the model to other dense crystalline rock types should be straightforward, requiring a standardized set of deformation experiments to determining the parameters outlined below. Extension of the model to other rock types may also be successful but will require proper verification. We expect that there will be some confining pressure range for porous sandstone over which this model will work successfully. For example, a representative stress-strain plot for Berea sandstone (18% porosity) is discussed in the appendix (Figure 14b). The basic shape of this deformation curve is remarkably similar to the shape of the granite tests used to develop the model.

Model parameters needed to evaluate (18) are as follows:

1. Three coefficients are needed to describe the failure envelope for Westerly granite; tensile strength, uniaxial compressive strength, and a third coefficient related to the increase in strength with confining pressure. In this way, we are able to represent the failure surface for Westerly granite over a confining pressure range from zero to 700 MPa. When less accuracy is required, a linearized Coulomb failure envelope would be adequate, requiring cohesive strength and coefficient of internal friction.

2. The model requires knowledge of the inelastic strain at peak stress, a quantity which is found to vary with confining pressure. A linear fit relating ε_0 to P_c requires two empirical coefficients.

3. A single shape factor α is used to relate stress to strain at constant strain rate, independent of confining pressure and strain rate.

4. The strain rate sensitivity of peak stress is an additional parameter needed for the model. For Westerly granite, this quantity a is nearly independent of confining pressure over the investigated range ($50 < P_c < 200$ MPa and 10^{-7} s$^{-1} < \dot{\varepsilon}_i < 10^{-5}$ s^{-1}).

Thus at room temperature seven parameters are needed for the model. An additional parameter (either Young's modulus or machine stiffness) is needed to include elastic deformation. This allows us to predict the general stress-strain-strain rate behavior of the rock from initial loading to failure (at approximately $\varepsilon_n = 1.1\varepsilon_0$). While we do not have full verification of the range of strain rate response, time to failure tests suggest that the model is applicable for strain rates from approximately 10^{-2} s^{-1} to 10^{-10} s^{-1}. This covers the range of strain rate normally encountered in quasi-static laboratory deforma-

tion experiments. Extrapolation to lower strain rates may be complicated by the activation of additional deformation mechanisms. Some laboratory data [*Lockner*, 1995, Figure 7] show consistent response to strain rates as high as 10^3.

To extend the model to temperatures above room temperature, additional parameters are needed. These include apparent activation energy $E \sim 90$ kJ mol^{-1}. In addition, the temperature dependence of a must be determined, requiring one additional parameter. It should be noted that the temperature dependence predicted by the model has not been verified. In fact, effects such as microstructural changes due to heating have not been considered in the model and may have an important effect on deformation characteristics. Also, once dislocation processes become important, new terms, reflecting these processes, would have to be added to the model. This is an area requiring future work.

The constitutive model developed in this paper relates a single (axial) component of principal strain and strain rate to principal stresses (σ_1, P_c) and temperature. A full treatment involving complete tensor quantities, even for a rock with axially symmetric mechanical properties, is beyond the scope of the present study, although, in principle, there are no technical limitations to carrying out such a study. Even so, the rheological model developed here provides a relatively simple tool for relating important thermomechanical quantities needed to characterize brittle deformation of rock.

Appendix

A1. Breakdown and Frictional Sliding Regions

Equation (17) expresses the stress-strain-strain rate relation for deformation of Westerly granite from initial loading to fault nucleation. Because strain is uniformly distributed in this deformation regime, applied boundary displacements can be easily related to the strain field within the sample. With fault formation and the accompanying drop in shear strength, strain is rapidly concentrated into the developing fault plane so that the strain field becomes highly heterogeneous. This process of fault formation and growth will ultimately lead to a regime of frictional sliding on a distinct fault plane. While we have not studied development of the breakdown region in detail, a complete description of deformation from initial loading to frictional sliding must deal with this transitional region. We present here data from a unique set of quasi-static deformation experiments on Westerly granite which have been discussed previously in the context of acoustic emission and microcrack growth [*Lockner et al.*, 1992a]. While these experiments were carried out at nominally constant acoustic emission rate, and not at constant strain rate, they can provide insight into the shape of the postnucleation failure envelope. Because deformation is heterogeneous in this transition phase, the deformation field is related to average axial shortening in a complex manner [*Lockner et al.*, 1991]. One basic result is shown in Figure 14a in which normalized stress-inelastic strain curves are plotted for a set of three granite experiments at 50 MPa confining pressure. Notice that the onset of fault nucleation occurs abruptly at ~10% past peak stress ($\varepsilon_i / \varepsilon_0 = 1.1$). Furthermore, the slope of the stress-strain curve following fault nucleation is highly repeatable and the weakening curve is linear over the observed range. These features cannot be seen in the smaller 25.4-mm-diameter sample experiments (i.e.,
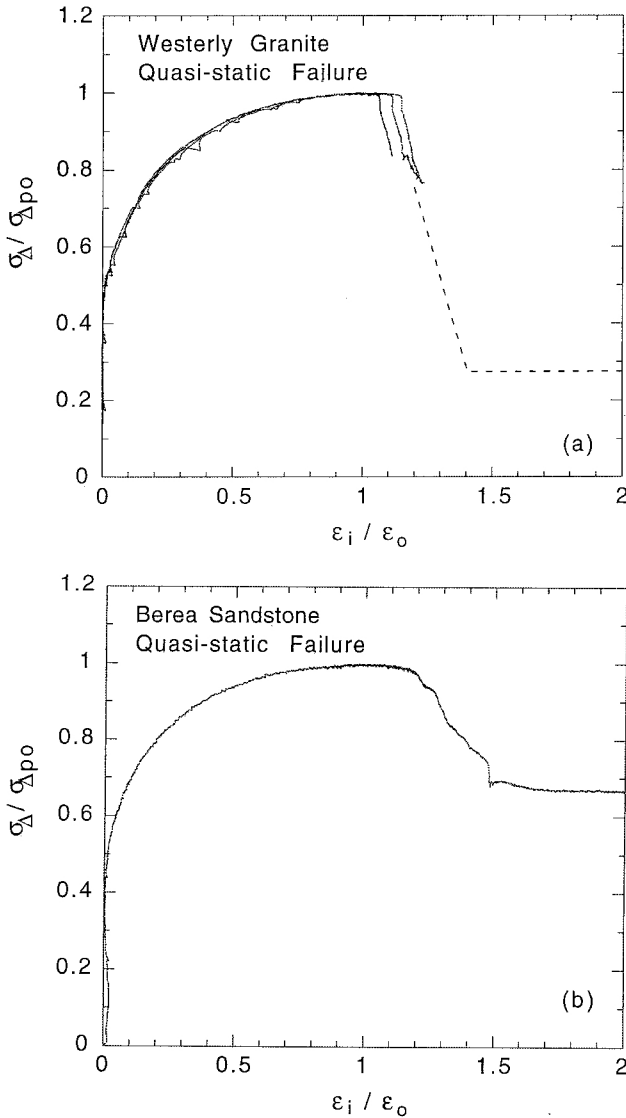
cases, the stress-strain curves flattened out before stress dropped to the frictional sliding strength. However, sandstone experiments from the same study formed faults at shallow angles and developed throughgoing faults without intersecting the steel end caps. An example of a complete sandstone stress-strain curve, from initial loading to frictional sliding, is shown in Figure 14b. In this case, the displacement weakening phase related to fault formation begins approximately 20% past peak stress. This breakdown phase is nearly linear until the frictional sliding stress is reached.

On the basis of these results we construct a representative failure curve for Westerly granite in which strength drops linearly with axial shortening from a characteristic strain at nucleation $\varepsilon_n = 1.1\,\varepsilon_0$ to a frictional sliding strength at a characteristic strain $\varepsilon_f = 1.4\,\varepsilon_0$. The failure curve is represented by dashed lines in Figure 14a and in Figures 10 and 11 assuming a coefficient of friction of 0.75 and a fault angle $\beta = 27°$. A complete deformation function for room temperature can now be defined as follows:

$$\sigma_\Delta = \sigma_{\Delta po}\,\sin^\alpha(\varphi)\left[1+a_0\ln\left(\frac{\dot{\varepsilon}_i}{\dot{\varepsilon}_0}\right)\right]$$

$$0<\frac{\varepsilon_i}{\varepsilon_0}\le 1.1 \qquad \text{(A1a)}$$

$$\sigma_\Delta = \left[\sigma_{\Delta n}-\left(\frac{\varepsilon_i-\varepsilon_n}{\varepsilon_f-\varepsilon_n}\right)(\sigma_{\Delta n}-\sigma_{\Delta f})\right]\left[1+a_0\ln\left(\frac{\dot{\varepsilon}_i}{\dot{\varepsilon}_0}\right)\right]$$

$$1.1<\frac{\varepsilon_i}{\varepsilon_0}\le 1.4 \qquad \text{(A1b)}$$

$$\sigma_\Delta = \sigma_{\Delta f}\left[1+a_0\ln\left(\frac{\dot{\varepsilon}_i}{\dot{\varepsilon}_0}\right)+b_0\ln\left(\frac{\theta}{\theta_0}\right)\right]$$

$$1.4<\frac{\varepsilon_i}{\varepsilon_0} \qquad \text{(A1c)}$$

Figure 14. (a) Normalized stress/inelastic strain curves for three quasi-static granite experiments at 50 MPa confining pressure. Constant acoustic emission rate rather than constant strain rate was used to control axial load and to prevent dynamic failure [see *Lockner et al.*, 1992]. In all cases, fracture nucleation was accompanied by an abrupt change in slope and rapid strength loss. Complete failure curve could not be followed because fracture propagated into end of sample and intersected steel loading piston. Dashed line indicates expected weakening to frictional sliding strength. (b) Complete normalized failure curve for Berea sandstone sample showing approximate linear weakening to frictional sliding strength.

where $\varepsilon_n = 1.1\,\varepsilon_0$; $\varepsilon_f = 1.4\,\varepsilon_0$; $\sigma_{\Delta n} = \sigma_{\Delta po}\sin^\alpha(1.1\pi/2)$; and $\sigma_{\Delta f}$ is determined from frictional properties. For example, for $P_c = 200$ MPa, $\beta = 30°$ and $\mu = 0.75$, equation (2) requires $\sigma_{\Delta f} = 611$ MPa. Here we have used the same a value for intact rock and frictional sliding. Where data exist, the frictional value a_{fric} can be modified appropriately. Following the developments of rate- and state-dependent friction laws, we have included in the friction law (A1c) a "state" variable θ which is proposed to evolve, for example, according to

$$\frac{\partial\theta}{\partial t}=1-\frac{\dot{\varepsilon}_i\theta}{\varepsilon^*} \qquad \text{(A2)}$$

where ε^* is a characteristic strain equivalent to D_c in standard rate- and state-dependent friction formulations. A proper discussion of rate- and state-dependent friction theory is beyond the scope of this paper. Interested readers are referred to the following references *Dieterich* [1978, 1979], *Ruina* [1980, 1998], *Rice and Gu* [1983], *Tullis and Weeks* [1985], *Blanpied et al.* [1995], *Perin et al.* [1995], *Beeler et al.* [1996], and *Blanpied et al.* [1998].

Figures 5a, 8b, and 9b) because once the fault nucleates, the sample becomes unstable and the slope of the unloading curve is controlled by machine stiffness. In the quasi-static acoustic emission experiments, the loading piston is actually backed off automatically in response to the change in acoustic emission rate before the sample becomes unstable.

In the granite experiments in which the fault was allowed to propagate, the failure plane formed at a steep angle to the sample axis so that the fault intersected the steel end cap before propagating completely across the sample. In these

A2. Comparison of a and a_{fric}

We have defined our deformation model in terms of axially oriented stresses and strains while friction analysis typically

uses a reference system based on a fault surface inclined at an angle β to the sample axis. Combining equations (2) and (A1a), shear and normal stress in the distributed deformation field are given by

$$\tau = \frac{1}{2}\sigma_{\Delta po}\sin(2\beta)\sin^{\alpha}(\varphi)\left[1 + a_0\ln\left(\frac{\dot{\varepsilon}_i}{\dot{\varepsilon}_0}\right)\right] \quad \text{(A3a)}$$

$$\sigma_n = P_c + \frac{1}{2}\sigma_{\Delta po}(1 - \cos(2\beta))\sin^{\alpha}(\varphi)\left[1 + a_0\ln\left(\frac{\dot{\varepsilon}_i}{\dot{\varepsilon}_0}\right)\right] \quad \text{(A3b)}$$

The algebraic expressions relating a_0 (defined in the axial reference frame) and a_{fric} (defined in fault reference frame) are cumbersome and not particularly revealing. For simplicity, we will provide two specific examples that demonstrate the correspondence between a_0 and a_{fric}. In the triaxial test geometry, both shear and normal stresses, resolved on a plane inclined at an angle to the sample axis, vary in an experiment run at constant confining pressure. Thus maintaining constant normal stress requires an adjustment in confining pressure. In the first example we evaluate stresses on a plane inclined at $\beta = 30°$, $P_c = 200$ MPa, $a_0 = 0.008$ and $\dot{\varepsilon}_i = \dot{\varepsilon}_0$ in an intact sample using the reference state values listed in Table 2. In this case, shear and normal stresses are 444.8 and 456.8 MPa, respectively. So that the coefficient of friction is $\mu = \tau/\sigma_n = 0.9737$. Increasing the strain rate by a factor of e while keeping normal stress constant requires a decrease in confining pressure to 198.7 MPa (equation (A3b)). The resulting shear stress is 447.0, or $\mu = 0.9786$. Thus, for $a_0 = 0.008$, we have $a_{fric} \cong (\Delta\mu_{\beta=30°}/\Delta\ln\dot{\varepsilon}_i) = 0.005$; a difference of ~38%.

As a second example, we evaluate stresses in the frictional sliding regime (equation (A1c)), assuming a reference state coefficient of friction $\mu_0 = 0.75$. $P_c = 200$ MPa requires shear and normal stresses of 264.6 and 352.7 MPa, respectively. Increasing strain rate by a factor of e and maintaining constant normal stress requires a decrease in confining pressure to 199.3. The resulting shear stress is 265.7, or $\mu = 0.7534$. In this case, for $a_0 = 0.008$, we have $a_{fric} = 0.0034$. Laboratory determinations of a_{fric} in artificial faults containing dry granite gouge range from about 0.003 to 0.009 [Blanpied et al., 1998].

References

Ashby, M. F., and S. D. Hallam, The failure of brittle solids containing small cracks under compressive stress states, *Acta Metall.*, *34*, 497-510, 1986.

Atkinson, B. K., (Ed.), *Fracture Mechanics of Rock*, 534 pp., Academic, San Diego, Calif., 1987.

Atkinson, B. K., and P. G. Meredith, The theory of subcritical crack growth with applications to minerals and rocks, in *Fracture Mechanics of Rock*, edited by B. K. Atkinson, pp. 111-166, Academic, San Diego, Calif., 1987.

Beeler, N. M., T. E. Tullis, M. L. Blanpied, and J. D. Weeks, Frictional behavior of large displacement experimental faults, *J. Geophys. Res.*, *101*, 8697-8715, 1996.

Blanpied, M. L., D. A. Lockner, and J. D. Byerlee, Frictional slip of granite at hydrothermal conditions, *J. Geophys. Res.*, *100*, 13,045-13,064, 1995.

Blanpied, M. L., C. J. Marone, D. A. Lockner, J. D. Byerlee, and D. P. King, Quantitative measure of the variation in fault rheology due to fluid-rock interactions, *J. Geophys. Res.*, 1998 *in press*.

Byerlee, J. D., Frictional characteristics of granite under high confining pressure, *J. Geophys. Res.*, *72*, 3639-3648, 1967.

Cruden, D. M., The static fatigue of brittle rock under uniaxial compression, *Int. J. Rock Mech. Min. Sci.*, *11*, 67-73, 1974.

Dieterich, J. H., Time-dependent friction and the mechanics of stick slip, *Pure Appl. Geophys.*, *116*, 790-806, 1978.

Dieterich, J. H., Modeling of rock friction, 1, Experimental results and constitutive equations, *J. Geophys. Res.*, *84*, 2161-2168, 1979.

Dieterich, J. H., Constitutive properties of faults with simulated gouge, in *Mechanical Behavior of Crustal Rocks, Geophys. Monogr. Ser., vol. 24*, edited by N. L. Carter et al., Washington, D. C., pp. 103-120, 1981.

Griggs, D. T., Creep in rocks, *J. Geol.*, *48*, 225-251, 1939.

Griggs, D. W., Experimental flow of rocks under conditions favoring recrystallization, *Geol. Soc. Am. Bull.*, *51*, 1001-1022, 1940.

Jaeger, J. C., and N. G. W. Cook, *Fundamentals of Rock Mechanics*, 593 pp., Chapman and Hall, New York, 1984.

Kilgore, B. D., M. L. Blanpied, and J. H. Dieterich, Velocity dependent friction of granite over a wide range of conditions, *Geophys. Res. Lett.*, *20*, 903-906, 1993.

Kranz, R. L., Crack-crack and crack-pore interactions in stressed granite, *Int. J. Rock Mech. Min. Sci. Geomech. Abstr.*, *16*, 37-47, 1979.

Kranz, R. L., The effects of confining pressure and stress difference on static fatigue of granite, *J. Geophys. Res.*, *85*, 1854-1866, 1980.

Kranz, R. L., Microcracks in rocks: A review, *Tectonophysics*, *100*, 449-480, 1983.

Kranz, R. L., and C. H. Scholz, Critical dilatant volume of rocks at the onset of tertiary creep, *J. Geophys. Res.*, *82*, 4893-4898, 1977.

Kranz, R. L., W. J. Harris, and N. L. Carter, Static fatigue of granite at 200°C, *Geophys. Res. Lett.*, *9*, 1-4, 1982.

Kuksenko, V., N. Tomilin, E. Damaskinskaya, and D. Lockner, A two-stage model of fracture of rocks, *Pure Appl. Geophys.*, *146*, 253-263, 1996.

Lockner, D. A., The role of acoustic emission in the study of rock fracture, *Int. J. Rock Mech. Min. Sci. Geomech. Abstr.*, *30*, 883-899, 1993a.

Lockner, D. A., Room temperature creep in saturated granite, *J. Geophys. Res.*, *98*, 475-487, 1993b.

Lockner, D. A., Rock failure, in *Rock Physics and Phase Relations: A Handbook of Physical Constants*, AGU Ref Shelf Ser., vol. *3*, edited by T. J. Ahrens, pp. 127-147, AGU, Washington, D. C., 1995.

Lockner, D. A., and J. D. Byerlee, Acoustic emission and creep in rock at high confining pressure and differential stress, *Bull. Seismo.l Soc. Am.*, *67*, 247-258, 1977.

Lockner, D. A., and J. D. Byerlee, Development of fracture planes during creep in granite, in *Proceedings, Second Conference on Acoustic Emission/Microseismic Activity in Geological Structures and Materials*, edited by H. R. Hardy and W. F. Leighton, pp. 11-25, Trans-Tech, Clausthal-Zellerfeld, Germany, 1980.

Lockner, D. A., and T. R. Madden, A multiple crack model of brittle fracture, 1, Non-time-dependent simulations, *J. Geophys. Res.*, *96*, 19623-19642, 1991a.

Lockner, D. A., and T. R. Madden, A multiple crack model of brittle fracture, 2, Time-dependent simulations, *J. Geophys. Res.*, *96*, 19643-19654, 1991b.

Lockner, D. A., R. Summers, and J. D. Byerlee, Effects of temperature and sliding rate on frictional strength of granite, *Pure Appl. Geophys.*, *124*, 445-469, 1986.

Lockner, D. A., J. D. Byerlee, V. Kuksenko, A. Ponomarev, and A. Sidorin, Quasi-static fault growth and shear fracture energy in granite, *Nature*, *350*, 39-42, 1991.

Lockner, D. A., J. D. Byerlee, V. Kuksenko, A. Ponomarev, and A. Sidorin, Observations of quasistatic fault growth from acoustic emissions, in *Fault Mechanics and Transport Properties of Rocks*, edited by B. Evans and T.-f. Wong, pp. 3-31, Academic, San Diego, Calif., 1992a.

Lockner, D. A., D. E. Moore, and Z. Reches, Microcrack interaction leading to shear fracture, in *33rd U.S. Rock Mechanics Symposium*, edited by J. R. Tillerson and W. R. Wawersik, pp.807-816, A. A. Balkema, Brookfield, Vt., 1992b.

Madden, T. R., Microcrack connectivity in rocks: A renormalization group approach to the critical phenomena of conduction and failure in crystalline rocks, *J. Geophys. Res.*, *88*, 585-592, 1983.

Moore, D. E., and D. A. Lockner, The role of microcracking in shear-fracture propagation in granite, *J. Struct. Geol., 17*, 95-114, 1995.

Mould, R. E., and R. D. Southwick, Strength and static fatigue of abraded glass under controlled ambient conditions, I, General concepts and apparatus, *J. Am. Ceram. Soc., 42*, 542-547, 1959.

Okui, Y., and H. Horii, Stress and time-dependent failure of brittle rocks under compression: A theoretical prediction, *J. Geophys. Res., 102*, 14,869-14,881, 1997.

Peng, S., and A. M. Johnson, Crack growth and faulting in cylindrical specimens of Chelmsford granite, *Int. J. Rock Mech. Min. Sci. Geomech. Abstr., 9*, 37-86, 1972.

Perin, G., J. R. Rice, and G. Zheng, Self-healing slip pulse on a frictional surface, *J. Mech. Phys. Solids, 43*, 1461-1495, 1995.

Reches, Z., and D. A. Lockner, Nucleation and growth of faults in brittle rocks, *J. Geophys. Res., 99*, 18159-18173, 1994.

Rice, J. R., and J. C. Gu, Earthquake aftereffects and triggered seismic phenomena, *Pure Appl. Geophys., 121*, 187-219, 1983.

Ruina, A. L., Friction laws and instabilities: A quasi-static analysis of some dry frictional behavior, Ph.D. thesis, Brown Univ., Providence, R. I., 1980.

Ruina, A. L., Slip instability and state variable friction laws, *J. Geophys. Res., 88*, 10359-10370, 1983.

Rutter, E. H., and D. H. Mainprice, The effects of water on stress relaxation of faulted and unfaulted sandstone, *Pure Appl. Geophys., 116*, 634-654, 1978.

Savage, J. C., J. D. Byerlee, and D. A. Lockner, Is internal friction friction?, *Geophys. Res. Lett., 23*, 487-490, 1996.

Scholz, C. H., Mechanism of creep in brittle rock, *J. Geophys. Res., 73*, 3295-3302, 1968a.

Scholz, C. H., Microfracturing and the inelastic deformation of rock in compression, *J. Geophys. Res., 73*, 1417-1432, 1968b.

Scholz, C. H., Static fatigue in quartz, *J. Geophys. Res., 77*, 2104-2114, 1972.

Tapponnier, P., and W. F. Brace, Development of stress-induced microcracks in Westerly granite, *Int. J. Rock Mech. Min. Sci. Geomech. Abstr., 13*, 103-112, 1976.

Tullis, T. E., and J. D. Weeks, Constitutive behavior and stability of frictional sliding of granite, *Pure Appl. Geophys., 124*, 384-414, 1985.

Tullis, J., and R. A. Yund, Experimental deformation of dry Westerly granite, *J. Geophys. Res., 82*, 5705-5718, 1977.

Wawersik, W. R., Time-dependent behavior of rock in uniaxial compression, in *14th Symposium, Rock Mechanics,* pp. 85-106, ASCE, 1973.

Wawersik, W. R., and C. Fairhurst, A study of brittle rock fracture in laboratory compression experiments, *Int. J. Rock Mech. Min. Sci., 7*, 561-575, 1970.

Wiederhorn, S. M., and L. H. Bolz, Stress corrosion and static fatigue of glass, *J. Am. Ceram. Soc., 53*, 543-548, 1970.

Wong, T.-f., Effects of temperature and pressure on failure and post-failure behavior of Westerly granite, *Mech. Mater., 1*, 3-17, 1982.

D. A. Lockner, U.S. Geological Survey, MS 977, 345 Middlefield Road, Menlo Park, CA 94025. (e-mail: dlockner@isdmnl.wr.usgs.gov)